Extreme Materials 2 (2026) 34–46

Contents lists available at ScienceDirect

Extreme Materials

journal homepage: www.keaipublishing.com/en/journals/extreme-materials/

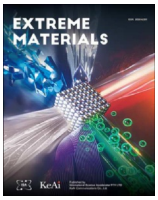

High-entropy titanate coating with superior high-temperature performance via atmospheric plasma spraying

Xiaofei Ma[a,b,c], Jinpeng Zhu[a,b,c,*], Chang Gao[a,b,c], Mingliang Li[a,b,c], Hailong Wang[a,b,c], Jilin He[a,b,c]

[a] *School of Materials Science and Engineering, Zhengzhou University, Zhengzhou 450001, China*
[b] *Zhongyuan Critical Metals Laboratory, Zhengzhou University, Zhengzhou 450001, China*
[c] *National Key Laboratory of Special Rare Metal Materials, Zhengzhou University, Zhengzhou 450001, China*

ARTICLE INFO

Keywords:
High-entropy ceramic coating
$(La_{0.3}K_{0.1}Ca_{0.2}Sr_{0.2}Ba_{0.2})TiO_{3+\delta}$
Atmospheric plasma spraying
Thermal protection performance
Failure mechanism

ABSTRACT

Thermal protection coatings for aerospace applications require robust mechanical properties, exceptional thermal insulation, and high impact resistance to safeguard critical hot-section components and thereby extend their service life. Previous studies have confirmed that high-entropy titanate $(La_{0.3}K_{0.1}Ca_{0.2}Sr_{0.2}Ba_{0.2})TiO_{3+\delta}$ (HE-LKTO) materials have excellent thermal protection properties and mechanical properties. To evaluate the viability of the HE-LKTO for Thermal protection coatings, a novel high-entropy titanate coating with a non-equimolar A-site composition was fabricated via atmospheric plasma spraying. The as-sprayed coatings subsequently underwent a comprehensive analysis of their microstructure and phase structure. Guided by the experimental results, the coating prepared under the optimized conditions was systematically investigated for its thermal protection performance via plasma flame thermal shock testing. The failure mechanism was revealed by analyzing the coating's dynamic behavior under extreme heat flux. Results show that the HE-LKTO coating prepared at 36 kW exhibits the optimal microstructure: the sprayed particles achieve complete melting and effective spreading, resulting in the lowest surface roughness and porosity. In addition, HE-LKTO coating maintains structural integrity at ablation temperatures of 1400 °C, exhibiting excellent high-temperature protection performance. At the extreme temperature of 1600 °C, however, the coating began to spall as a result of accumulated thermal stress induced by the mismatched thermal expansion coefficients between the coating and substrate, as well as crack propagation along interlamellar boundaries and interface separation. This work not only validates the great potential of HE-LKTO as thermal protection coatings but also provides crucial insights into its failure mechanism, laying a foundation for future performance enhancement.

1. Introduction

Thermal protection coatings (TPCs) are critical materials designed for extreme high-temperature environments, aiming to provide effective protection for key high-temperature components [1–3]. TPCs with excellent performance not only reduce the operating temperature of substrates, but also significantly prolong their service life. Currently, yttria-stabilized zirconia (YSZ) remains the most widely utilized TPC material due to its relatively low thermal conductivity (2.6 $W \cdot m^{-1} \cdot K^{-1}$ at 1200 °C) and balanced mechanical properties [4,5]. However, its sustained operational limit is approximately 1200 °C. Exposure to temperatures beyond this threshold induces phase transformations in YSZ, accompanied by volumetric expansion, which ultimately leads to coating cracking and spallation. As a result, these constraints have driven the advancement of next-generation TPCs materials, for which essential criteria include superior high-temperature performance, reduced thermal conductivity, and a thermal expansion coefficient compatible with the underlying substrate [6].

Actually a new class of high-entropy ceramic coating, with excellent high-temperature performance [7], lower thermal conductivity [8] and a matching coefficient of thermal expansion [9], is anticipated to provide new breakthroughs for the high temperature protection field [10]. Since Rost et al. [11] proposed the concept of entropy-stabilized oxides in 2015, high-entropy ceramic coatings have experienced rapid development. It should be noted that high-entropy ceramic coating is a new type of ceramic coating material composed of five or more main metal or non-metal elements, forming a solid solution phase with a single stable crystal structure [12]. While equimolar or near-equimolar ratios are typically employed to maximize configurational entropy, the definition of high-entropy ceramics has

---

[*] Corresponding author at: School of Materials Science and Engineering, Zhengzhou University, Zhengzhou 450001, China.
E-mail address: zhujinpeng@zzu.edu.cn (J. Zhu).

https://doi.org/10.1016/j.exm.2026.01.002
Received 26 November 2025; Received in revised form 7 January 2026; Accepted 7 January 2026

expanded to include materials composed of at least four principal elements with either near-equimolar or non-equimolar compositions, which occupy one or more Wyckoff positions [10]. Thanks to the four core effects (high-entropy effects [13], sluggish diffusion effects [14], lattice-distortion effects [15], and cocktail effects [16]) of high-entropy ceramic coatings, they possess excellent combined properties and have become promising candidates for advanced TPCs. Wu et al. [17] successfully fabricated two types of high-entropy titanate ceramics via an in-situ solid-phase reaction method. Their study revealed that the single-phase ceramic (Mg, Co, Ni, Zn)Ti_2O_5 exhibits exceptional thermophysical properties due to its ultra-high configurational entropy. Similarly, Zhu et al. [18] produced a high-entropy rare-earth titanate coating $(Y_{0.2}Gd_{0.2}Ho_{0.2}Er_{0.2}Yb_{0.2})_2Ti_2O_7$ using APS that shows excellent thermal insulation performance and high-temperature stability, making it promising for aero-engine applications. In fact, conventional perovskite titanates such as $SrTiO_3$, $BaTiO_3$, and their doped variants have been investigated as TPCs or environmental barrier coatings due to their attractive thermoelectric properties [19] and excellent mechanical features [20] at high temperatures. Hanifi et al. [21] successfully prepared an aluminum titanate ceramic coating (Al_2O_3–40 %TiO_2) using the APS technique and explicitly pointed out that Al_2O_3–40 %TiO_2 is one of the most important ceramic materials widely used in TPCs, which protect metallic components in industrial and aircraft gas turbine engines under high-temperature conditions. However, the introduction of high-entropy design into titanate systems represents a significant advancement. Earlier studies by our group [22] confirmed that the $(La_{0.3}K_{0.1}Ca_{0.2}Sr_{0.2}Ba_{0.2})TiO_{3+\delta}$ (HE-LKTO) exhibit exceptional intrinsic properties: a low thermal conductivity of 1.46 $W{\cdot}m^{-1}{\cdot}K^{-1}$ at 1200 ℃ (44 % lower than YSZ), a high thermal expansion coefficient of 12.2×10^{-6} K^{-1} at 1200 ℃ (well-matched with nickel-based alloys), and excellent mechanical properties (Vickers hardness of 11.5 GPa). The multi-component composition of HE-LKTO material leads to enhanced phonon scattering, reduced thermal conductivity and improved phase stability—properties that are not achievable with conventional titanates.

Atmospheric plasma spraying (APS) has emerged as the favored approach for implementing HE-LKTO as TPC, owing to its combination of high deposition efficiency, cost-effectiveness, and compatibility with large-scale components [23–26]. Zhang et al. [27] successfully synthesized a $(Y_{0.2}Yb_{0.2}Ho_{0.2}Er_{0.2}Tm_{0.2})_2Hf_2O_7$ coating using the APS. They pointed out that the APS-fabricated coating exhibits a lamellar structure with porosity, which further reduces heat transfer and thereby leads to good thermal insulation performance. Zhu et al. [6] prepared a novel high-entropy rare-earth aluminate $(Y_{0.2}Yb_{0.2}Lu_{0.2}Eu_{0.2}Er_{0.2})_3Al_5O_{12}$ coating on a nickel-based superalloy via APS, systematically evaluated its thermal shock performance, and revealed the coating's failure mechanism in actual high-temperature environments. Currently, the studies on high-entropy titanate TPCs fabricated via APS is limited, while the research primarily focused on bulk and powder materials [22,28–30]. Detailed reports on the microstructural characteristics and thermal protection performance of such coatings remain scarce. Therefore, a systematic investigation into the influence of key APS parameters on the microstructure and properties of the coatings is of great importance. Such efforts not only facilitate a deeper exploration of the deposition mechanisms of high-entropy titanates, but also pave the way for achieving desirable coating properties, thereby advancing their practical deployment in thermal protection systems for critical high-temperature equipment.

This study is driven by a high-entropy material design strategy, with the objective of applying a novel high-entropy titanate coating in the field of thermal protection. HE-LKTO coatings were deposited on nickel based alloy substrates (with NiCrCoAlY bonding layer) by changing the spraying power using APS technology, and the phase composition as well as microstructure of the coatings were characterized to screen for the optimal spraying parameters. Furthermore, plasma flame thermal shock testing were conducted on the HE-LKTO coating prepared under the optimal spraying parameters to evaluate the thermal protection performance of the coating. Ultimately, the thermal protection capability of the HE-LKTO coating was assessed by examining its phase stability and microstructural evolution following thermal shock tests. This study not only validates the potential of HE-LKTO as an advanced TPC but also provides fundamental insights into its failure mechanisms under extreme thermal conditions, laying a groundwork for future performance optimization and engineering applications.

2. Material and methods

2.1. Preparation of HE-LKTO powders and coatings

High-purity (> 99.5 %) powders (La_2O_3, K_2CO_3, CaO, SrO, BaO and TiO_2 from Shanghai Macklin Biochemical Co., Ltd., China.) were employed as starting materials and weighed according to the stoichiometric ratio. The blended powders were suspended in anhydrous ethanol and subjected to attrition milling for 12 h at a speed of 300 r/min, employing zirconia balls as the grinding media. After mixing, the powder suspension was processed by rotary evaporation to yield a uniformly dry powders. Following calcination at 900 ℃ for 3 h, the resulting powders were classified through a 200-mesh sieve. The powders were subjected to pressure-free sintering at 1400 ℃ for 10 h, under conditions of a heating rate of 5 ℃/min. HE-LKTO powders were blended with an aqueous solution containing 4.5 wt% polyvinyl alcohol (PVA) and 1 wt% dispersant at a weight ratio of 6:4. The mixture was then transferred into a grinding tank and subjected to ball milling for 5 h to obtain a homogenized slurry. The slurry was sprayed in a spray granulation device (YC-019, Shanghai Ya Cheng Instrument Equipment Co., Ltd., China) with an atomizing pressure of 0.15 MPa and a inlet temperature of 240 ℃ to produce spherical powders. The powder was sintered at 650 ℃ and 1050 ℃ (3 h each) to both remove organic additives and improve its cohesive strength. Fig. 1 shows the microstructure and XRD pattern of HE-LKTO spheroidized powders after heat treatment. After heat treatment, the HE-LKTO granular powders still maintain excellent surface smoothness and intact apple like morphology (as shown in Fig. 1(a)). This unique internal concave structure is formed by the direct evaporation of solvent from the interior of the droplet. During the particle transformation process in droplets, the evaporation rate is effectively suppressed by forming a flexible shell with extremely low permeability [31]. This spray granulating powder has excellent physical properties, its fluidity is 60 s/50 g, and its apparent density is 1.73 g/cm^3. By comparing the XRD pattern (Fig. 1(b)), it was found that the heat treatment did not change the crystal structure, while the EDS mapping (Fig. 1(d)) further confirmed the uniform distribution of the metal composition. The particle size distribution of these granular powders is suitable for APS, as evidenced by the data in Fig. 1(c): D_{50} is 39.57 μm, D_{90} is 48.95 μm, and the average diameter is 41.61 μm, all of which are within the recommended range of 30–80 μm [27]. These results indicate that spheroidized powders have extremely high structural stability under high temperature conditions and meet the basic requirements of APS for raw materials.

Prior to spraying, the circular nickel-based alloy substrate (diameter: 25 mm, thickness: 2 mm) surface was roughened to a roughness exceeding 5 μm using a box-type sandblasting machine (HC-9080, Shijiazhuang Hongchen Machinery Co. Ltd., China). The substrate was subsequently subjected to ultrasonic cleaning in acetone for 5 min for the purpose of eliminating residual particulate contaminants from the surface. In order to further improve the deposition efficiency of the coating, a metal bonding transition layer (NiCrCoAlY) with a thickness of about 80 μm was prepared on the substrate surface using APS in advance. The HE-LKTO coating was finally sprayed at powers of 30 kW, 33 kW, and 36 kW, named HE-LKTO-1, HE-LKTO-2, and HE-LKTO-3 respectively, with three sets of replicate samples prepared for each spraying power. The detailed parameters are shown in Table 1.

2.2. Microstructural characterization of HE-LKTO coatings

The phase structure of the HE-LKTO coatings were determined by X-ray diffractometry (XRD, NSW, The Netherlands). The microstructural

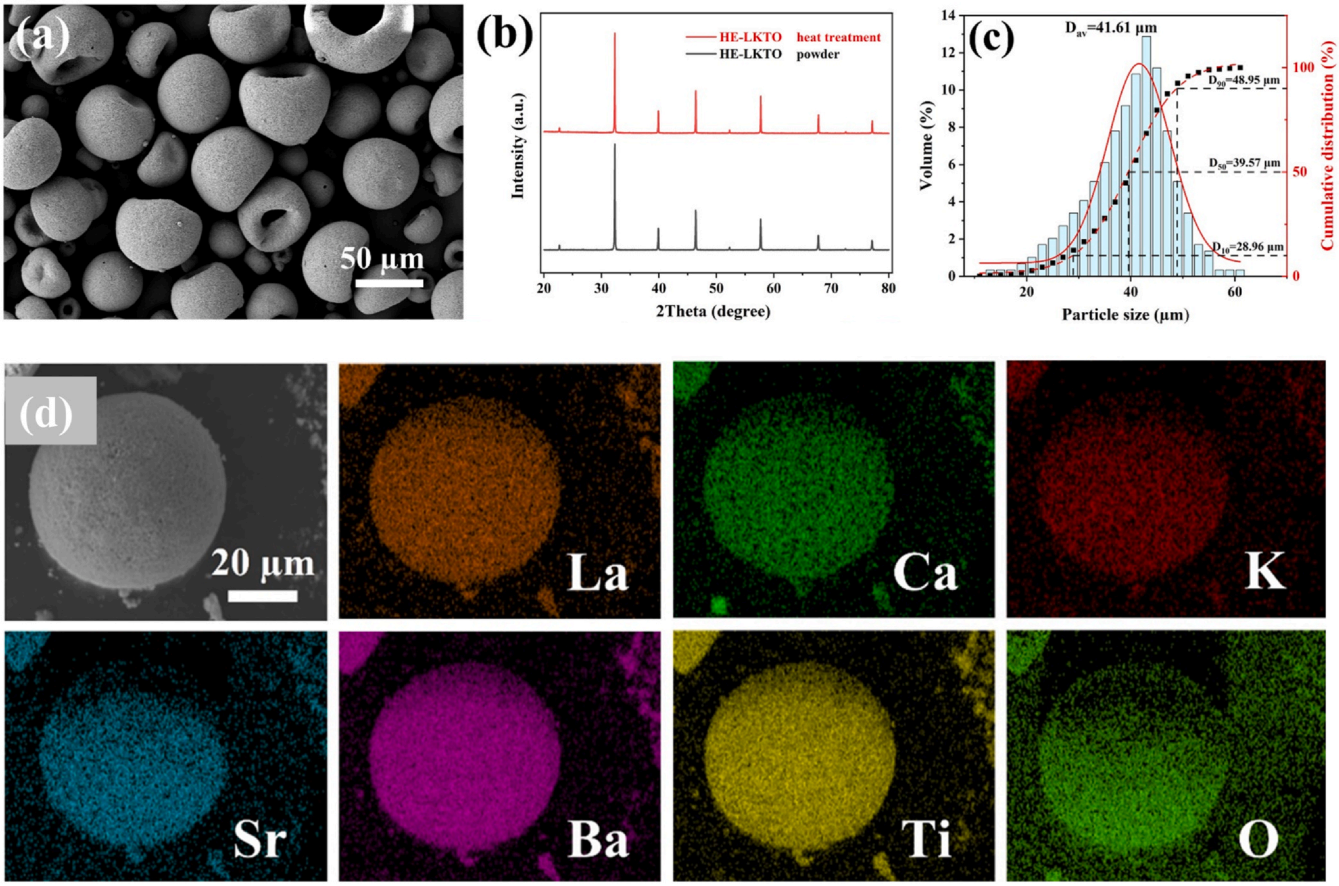

Fig. 1. Microscopic morphology (a), XRD pattern (b), particle size distributions (c), and elemental distribution map (d) of HE-LKTO granulated powder after heat treatment.

Table 1
Parameters for preparing bonding layer and HE-LKTO coatings by APS.

Samples	Spray distance (mm)	Primary gas Ar (slpm)	Secondary gas H_2 (slpm)	Carrier gas N_2 (slpm)	Current (A)	Spray power (kW)
NiCrCoAlY	100	33.3	5.0	3.3	500	30
HE-LKTO-1	100	33.3	5.0	3.3	500	30
HE-LKTO-2	100	33.3	6.7	3.3	520	33
HE-LKTO-3	100	41.7	8.3	3.3	550	36

morphology and elemental distribution of the coatings were characterized using a scanning electron microscope (SEM, NOVANanoSEM 230 FEI, USA) equipped with an energy-dispersive spectroscopy (EDS) system. The surface roughness of the coatings were observed using atomic force microscopy (AFM, Bruker Dimension Icon, Germany).

2.3. *Thermal shock test of HE-LKTO coatings*

The thermal insulation performance and resistance to extreme heat flow erosion of the HE-LKTO coating were evaluated using a high-temperature plasma flame flow thermal shock test platform independently built in the laboratory. The coating sample (φ 25 mm × 3 mm) was mounted in a graphite fixture on the experimental platform. The testing distance was set at 60 mm, and the front surface of the sample was heated to the target temperature by adjusting the process parameters of the APS system. During the testing process, the surface and backside temperatures of the HE-LKTO coating were monitored in real-time using infrared thermography (HA384) and thermocouples, respectively. The coating surface was heated to target temperatures of 1000 °C, 1200 °C, 1400 °C, and 1600 °C, respectively, and held at each temperature for 300 s before the plasma torch was retracted, marking the end of the evaluation cycle. A schematic of the high-temperature plasma flame flow thermal shock test platform is shown in Fig. 2. The mass of the HE-LKTO coatings was measured using an analytical balance (Zhuojing Corp., BSM-220.4) before and after thermal shock testing to determine the coating mass loss. The reported values are calculated based on three independent repeated samples at each temperature.

3. Results and discussions

3.1. *Phase analysis and microstructure of the HE-LKTO coatings*

The phase composition of the HE-LKTO coatings were examined by XRD to confirm that the as-sprayed powders did not undergo phase transition during the APS process. As shown in Fig. 3, the HE-LKTO coatings deposited at different power levels all exhibit diffraction peaks matching those of the sprayed powder, confirming a perovskite structure [22]. A comparison of the XRD patterns reveals a significant reduction in diffraction peak intensity for the HE-LKTO coatings compared to the as-sprayed powders. This reduction can be attributed to the low crystallinity resulting from the short processing time and rapid solidification characteristic of the APS process [32].

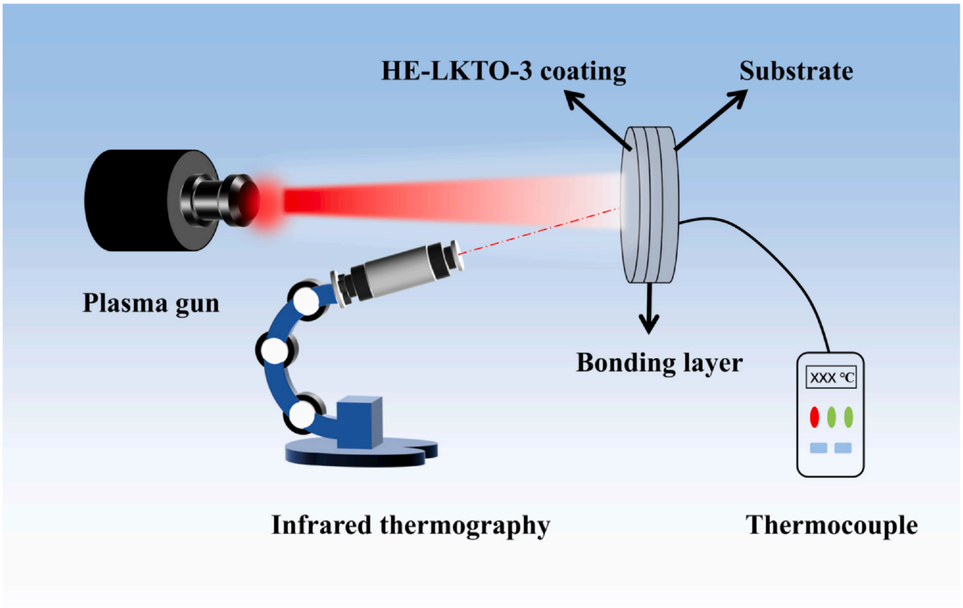

Fig. 2. Schematic diagram of plasma flame thermal shock experimental platform.

To further investigate the microstructures of the HE-LKTO coatings under different powers, SEM, EDS, and AFM analyses were utilized. As shown in Fig. 4(a), when the spraying power is 30 kW (HE-LKTO-1 coating), there are many irregular particles and some incompletely melted spherical particles on the surface of coating. This occurred because the low power only melted the spherical powder into a liquid state on the outside, while the core remained an unmelted solid particle. When these incompletely melted spherical powders collide with the substrate at a certain speed, the internal unmelted particles may break and form many small particles. Consistent with this analysis, the AFM images (Fig. 4(a1) - (a2)) indicated a rough and inhomogeneous surface for the HE-LKTO-1 coating. With the increase of spraying power to 33 kW (HE-LKTO-2 coating), as shown in Fig. 4(b), the melting degree of coating particles has been greatly improved, and the coating surface is relatively flat. The increase in spraying power led to a higher particle heating temperature in the plasma flame, thereby promoting particle melting. Nevertheless, some partially melted particles, along with a few microcracks and pores, were still present. To further enhance particle melting and explore the effect of power on coating microstructure, the spray power was increased to 36 kW (HE-LKTO-3 coating). As shown in Fig. 4(c), compared with the coating prepared at low power, the HE-LKTO-3 coating has a smoother, flatter, and denser surface (as shown in Fig. 4(c1) - (c2)). It should be noted that in order to better observe the micro-scale smoothness within the well-formed sputtered area of the coating, the AFM measurements were conducted on a local region of 5 × 5 μm. Therefore, the obtained roughness value cannot represent the overall surface roughness of the coating, but this does not affect the observation of the roughness variation trend. Furthermore, the EDS mapping in Fig. 4(d) reveals that the HE-LKTO-3 coating prepared at 36 kW exhibits a homogeneous distribution of all elements, with no detectable segregation.

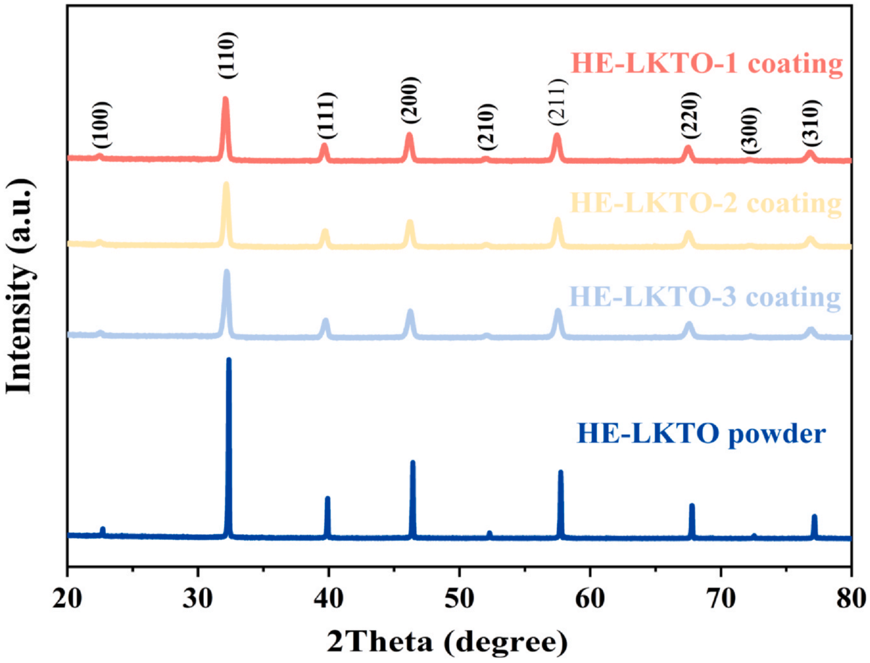

Fig. 3. XRD patterns of HE-LKTO coatings deposited under different spraying powers.

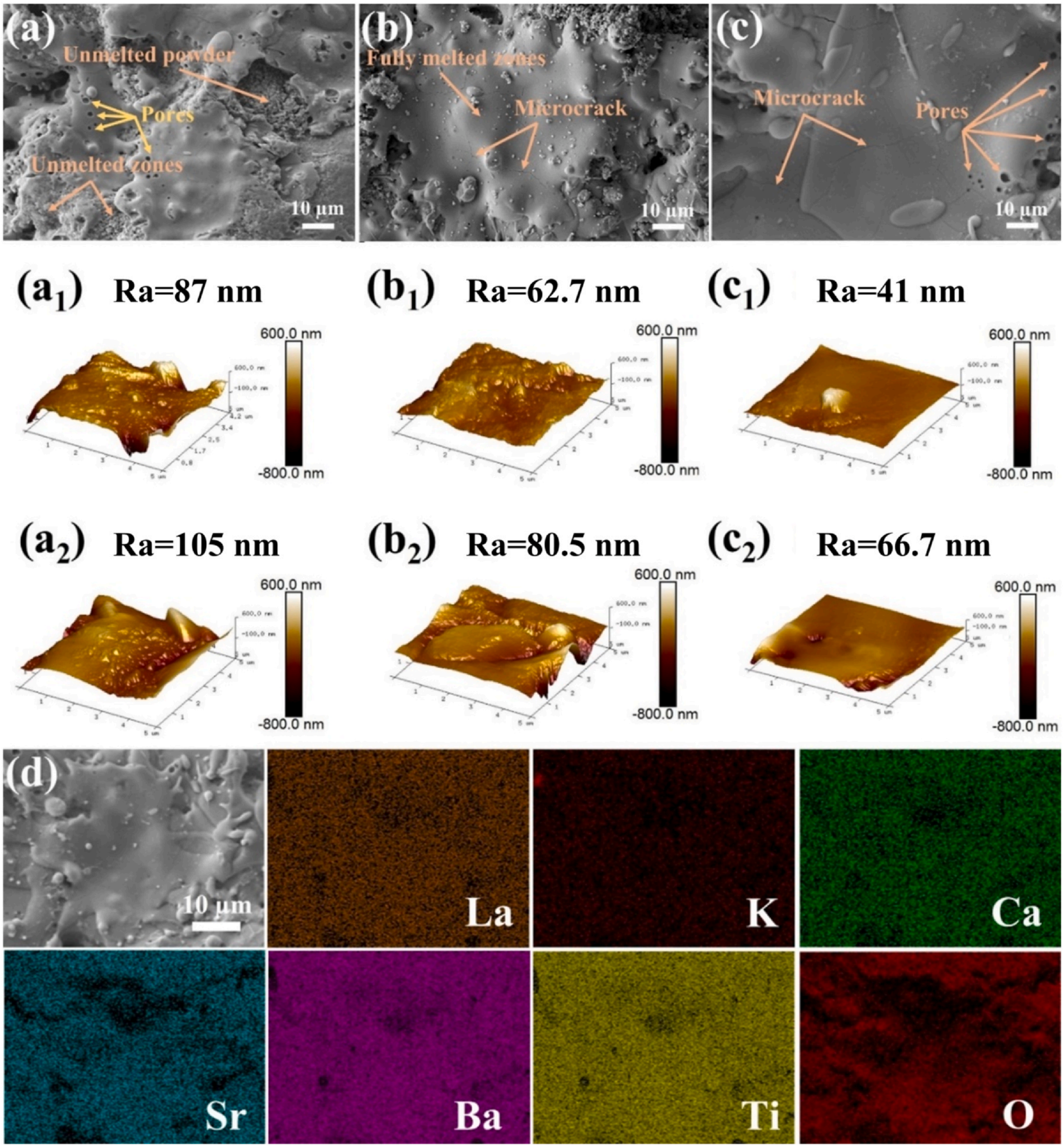

Fig. 4. Surface microstructural characteristics of HE-LKTO coatings under different spraying powers: (a) SEM image at 30 kW, (a1)-(a2) AFM images (5 × 5 μm scan area) at 30 kW; (b) SEM image at 33 kW, (b1)-(b2) AFM images (5 × 5 μm scan area) at 33 kW; (c) SEM image at 36 kW, (c1)-(c2) AFM images (5 × 5 μm scan area) at 36 kW; (d) SEM image and elemental distribution maps of the HE-LKTO coating surface at 36 kW.

It can be clearly seen from Fig. 5 that the cross-sectional thickness and morphology of HE-LKTO coating vary with different spray powers. All cross-sections exhibit a distinct three-layer structure, with the average thickness of HE-LKTO-1, HE-LKTO-2, and HE-LKTO-3 coatings being 173.42 μm, 186.51 μm, and 216.23 μm, respectively, while the corresponding average thickness of the bonding layer is 85.76 μm, 84.85 μm, and 83.12 μm, respectively. It can be concluded that the coating thickness significantly increases with the increase of spraying power, while the bonding layer thickness remains basically unchanged. The increase in thickness is attributed to the more complete melting of high-entropy titanate particles at higher power, which improves deposition efficiency and leads to the formation of more material deposits on the substrate [33]. As shown in Fig. 5(a), the HE-LKTO-1 coating deposited at a power of 30 kW exhibits a porous and loose structure due to its low power. When the power is low, it can lead to insufficient spreading of the coating when the molten particles collide with the substrate, resulting in the formation of pores during the cooling shrinkage process and adversely affecting the bonding strength of the coating [34]. As the power gradually increased to 33 kW (HE-LKTO-2) and then to 36 kW (HE-LKTO-3), the pores observed in the cross-section of the coating gradually decreased. According to ImageJ software analysis, the measured porosity of HE-LKTO coating is 15.38 %, 9.89 %, and 6.21 %, corresponding to three different spraying powers (30 kW, 33 kW, and 36 kW). In summary, HE-LKTO-3 coating has a high-quality microstructure with a few pore defects, which meets the key application requirements as a TPC. As shown in Fig. 5(d), the fracture surface of HE-LKTO-3 coating exhibits a typical layered structure. In addition, a small number of pores and globular voids can be observed in the microstructure, which is a characteristic of the APS manufacturing process itself [35]. This occurs as the plasma-melted droplets travel at high speed to the metal substrate, enveloping some surrounding air. The subsequent rapid solidification of these droplets on the substrate prevents the timely escape of the trapped air, thereby leading to the formation of pores and voids [36,37]. In fact, these defects are beneficial

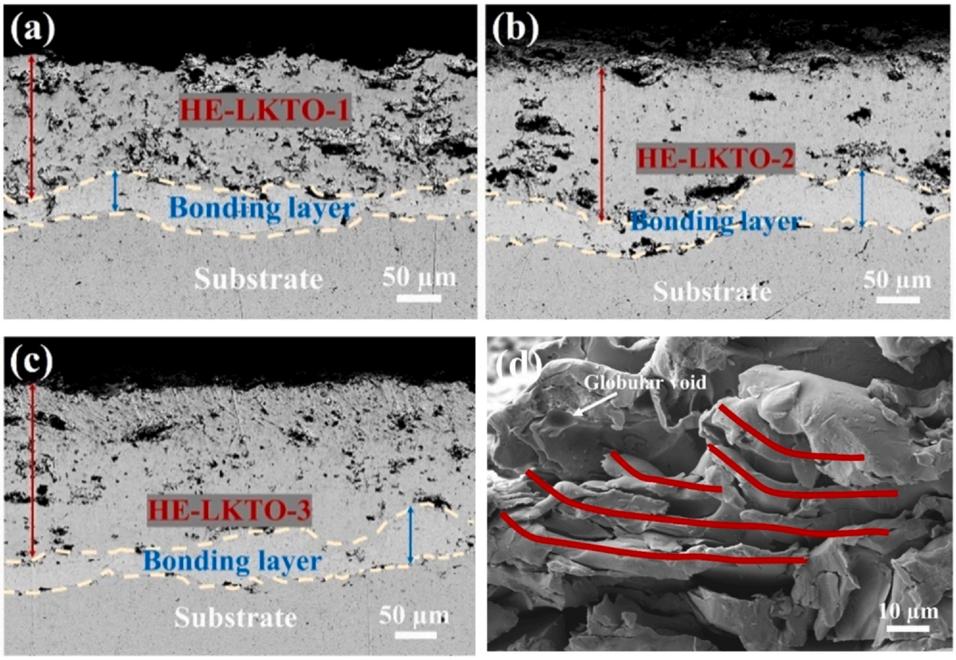

Fig. 5. Cross-sectional morphology of the HE-LKTO coatings deposited at different spraying powers: (a) 30 kW; (b) 33 kW; (c) 36 kW, and fracture surface morphology (d) of the HE-LKTO-3 coating.

to some extent, as they help relieve stress during thermal cycling and thereby improve the thermal protection performance. Huang et al. [38] employed a combination of the quartet structure generation set methods and Monte Carlo simulation methods to develop a thermal analysis model for TPCs. This study found that microcracks reduce the thermal conductivity of coatings with different structures, thereby improving their thermal insulation performance to some extent. Therefore, the HE-LKTO-3 coating achieves a balanced performance: its low porosity ensures adequate bonding strength and erosion resistance, while its inherent lamellar structure and the presence of limited microcracks still provide essential pathways for stress relief and thermal insulation.

3.2. *Thermal ablation behavior of the HE-LKTO-3 coating*

Based on the aforementioned analysis, the HE-LKTO-3 coating exhibits the most optimal microstructure, the lowest porosity, and the most compact structure. Therefore, thermal shock tests were conducted specifically on the HE-LKTO-3 coating. In this study, a plasma spraying flame was selected as the high-temperature heat source.

Compared with traditional thermal shock testing sources such as butane flames, plasma flames have higher center temperatures and stronger impact forces, providing key reference value for accurately evaluating the performance of coatings under actual usage conditions. As shown in Fig. 6(a), after 300 s of thermal shock ablation at 1000 ℃, the HE-LKTO-3 coating showed no signs of thermal shock damage, indicating that the coating maintained its integrity and structural stability at that temperature. After the ablation temperature was raised to 1200 ℃ and lasted for 300 s, the HE-LKTO-3 coating did not show significant thermal shock damage, only a small amount of ablation marks were observed, and the overall coating remained highly intact. When the ablation temperature further increased to 1400 ℃, a large number of dark spots (ablation points) began to appear in the ablation area at the center of the coating surface, although the entire coating still maintained a relatively high flatness. At the ablation temperature of 1600 ℃, a large number of ablation points initially appeared on the surface of the coating, and their range gradually expanded. After the ablation operation lasted for 180 s, some areas of the coating began to peel off. Subsequently, the substrate of the central ablation area was rapidly damaged, leading to melting and collapse, ultimately resulting in sample failure. The XRD pattern (Fig. 6(b)) shows that the phase composition of the surface ablation area is consistent with that of the HE-LKTO-3 coating, and no secondary or impurity phases were formed during the high-temperature plasma flame ablation process. This excellent phase stability is supported by the fundamental “high-entropy effects”, specifically the high configurational entropy and severe lattice distortion. The significantly increased configurational entropy of multicomponent systems effectively reduces Gibbs free energy, making it thermodynamically more favorable for the formation and stabilization of single-phase solid solutions [39,40]. Meanwhile, significant atomic size differences between constituent elements can lead to severe lattice deformation, resulting in significant energy barriers that impede atomic diffusion and phase separation [41–43]. It is this synergistic effect that enables HE-LKTO-3 coating to maintain excellent high-temperature stability even after undergoing thermal ablation processes. Additionally, as the plasma jet generated by the APS system is a high-velocity gas flow containing ionized species, it exerts an impact on the coating surface. Therefore, the mass loss of the HE-LKTO coatings before and after thermal shock are listed in Table 2. As can be seen from Table 2, the mass loss of the coating gradually increases with the progressive rise of the thermal exposure temperature. This is due to the fact that at higher temperatures, the thermal expansion mismatch between the coating and the substrate becomes more pronounced, generating greater interfacial stress and accelerating crack initiation and propagation. Simultaneously, high temperatures soften the coating surface, thereby reducing its resistance to the high-velocity impact and shear forces imposed by the plasma jet. The aforementioned factors collectively degrade the coating’s cohesion and erosion resistance, leading to increased mass loss under higher thermal loads.

The microstructures of the ablated coatings were analyzed using SEM and EDS to further link it with thermal protection performance. The study on microstructural characteristics mainly focused on the analysis of coatings exposed under conditions of 1200 ℃, 1400 ℃, and 1600 ℃. The reason for choosing this group of samples is that all the coatings subjected to impact treatment have the same phase composition, and the macroscopic morphology of the coating at 1000 ℃ has not undergone any changes (as shown in Fig. 6(a)). Fig. 7 shows the surface morphology of HE-LKTO-3 coating after exposure to a plasma jet at

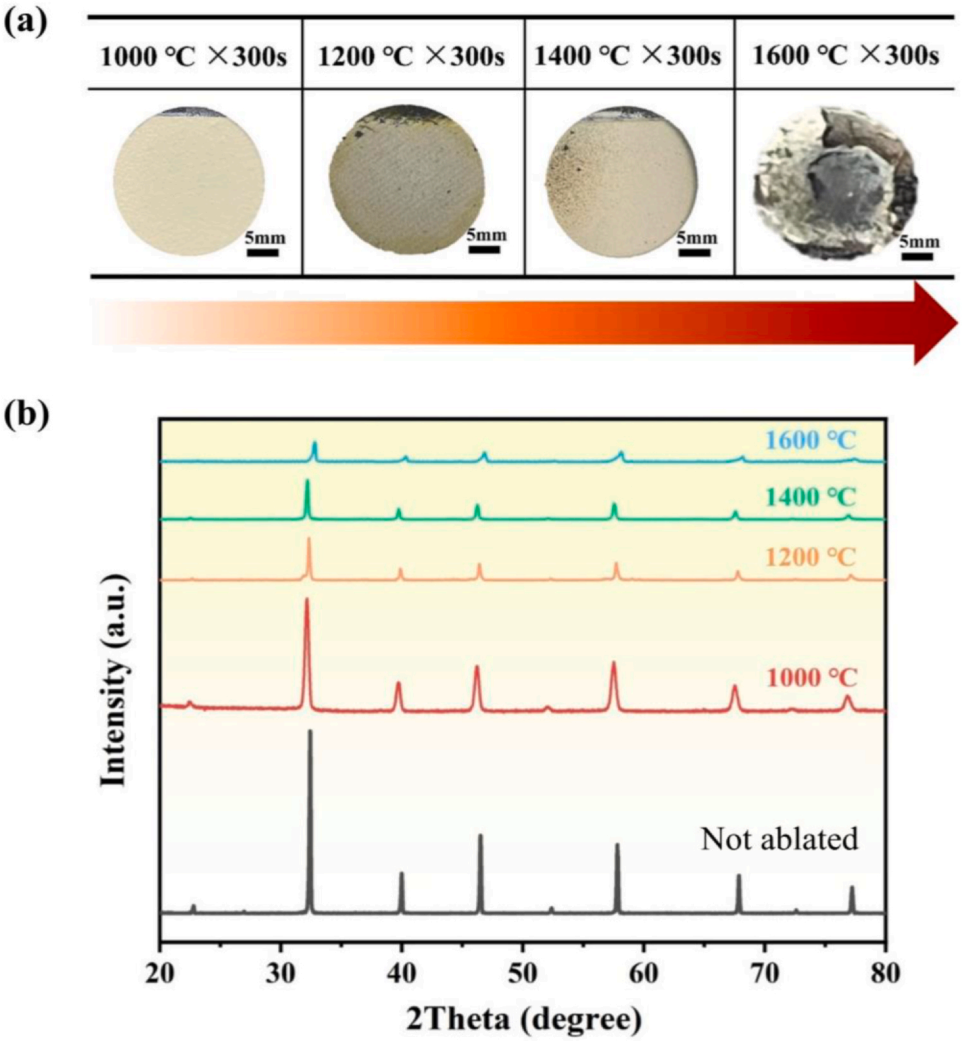

Fig. 6. Macroscopic morphology (a) and XRD patterns of the HE-LKTO-3 coating after ablation for 300 s at different temperatures.

1200 °C. In the central ablation area (as shown in Fig. 7(b)), a large number of pits and particle aggregates can be observed, which is attributed to the continuous erosion effect under high-temperature plasma flow. The degree of ablation in the transitional ablation zone (as shown in Fig. 7(c)) exhibits a significant gradient change: the area not directly exposed to the jet maintains its original shape, while the area directly exposed to thermal radiation undergoes ablation. This leads to the formation of micropores and cracks. In the peripheral ablation area (as shown in Fig. 7(d)), the coating surface remained largely unchanged because the plasma jet with Gaussian energy distribution significantly reduced the heat flux density at the edge, resulting in only a slight ablation effect [44,45]. During the testing process, thermal stress was generated due to the steep temperature gradient on the coating surface. When the plasma jet stops, rapid surface cooling leads to local heat accumulation, resulting in stress concentration and the formation of large areas of microcracks [9]. It is worth noting that crack propagation is an effective heat dissipation pathway, which alleviates stress gradients through the distribution of heat flux [38]. EDS mapping was conducted in the transition zone between central ablation and peripheral regions to analyze elemental redistribution across the thermal gradient. As shown in Fig. 7(f), after plasma jet testing at 1200 °C, the A-site metal elements in the HE-LKTO-3 coating maintained a highly uniform distribution, and no element separation phenomenon was detected.

Fig. 8 shows the surface morphology of HE-LKTO-3 coating after exposure to 1400 °C plasma jet. As shown in Fig. 8(b), the central ablation area is filled with holes and deep pits, which are typical features of thermal damage. The formation of these deep pits is due to the exposure of the area to higher temperatures and stronger plasma flow impacts. In addition, due to the highly concentrated heat flux, the cooling process of the material is relatively slow, providing sufficient time for grain growth [18]. Therefore, smaller spherical grains gradually thicken, forming tightly arranged grain aggregates. In the transitional ablation zone (Fig. 8(c)), the surface remains relatively flat compared to the central ablation zone, and the ablation effect is weaker. However, the peripheral ablation area (Fig. 8(d)) did not show significant structural changes. This spatial difference arises from the Gaussian energy distribution of the plasma jets, in which the heat flux

Table 2
Mass loss of the HE-LKTO coatings after thermal shock tests at different temperatures.

Temperature (°C)	1000	1200	1400	1600
Mass loss (g)	0.0002 ± 0.0001	0.0061 ± 0.0008	0.0154 ± 0.0013	0.1132 ± 0.0217

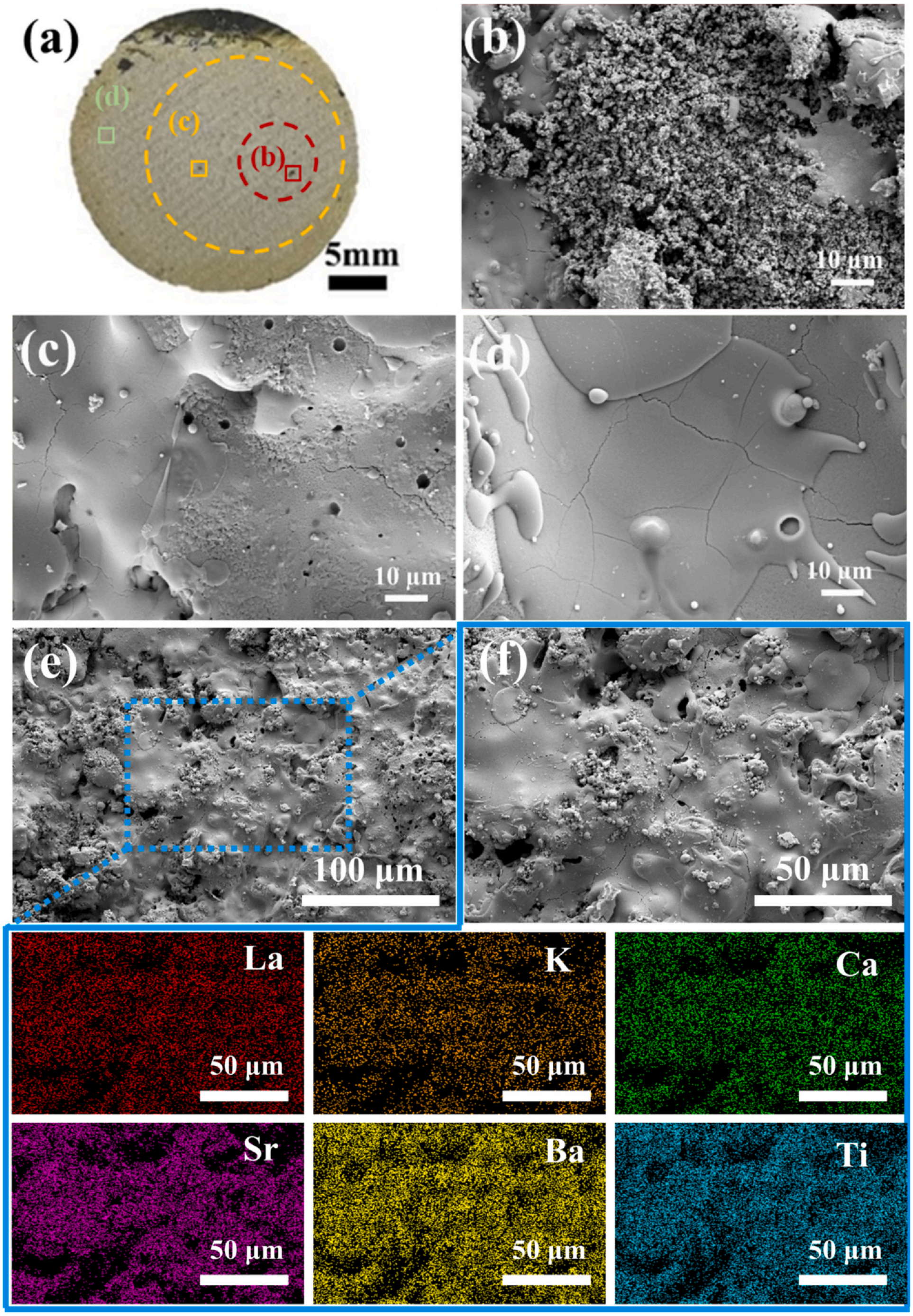

Fig. 7. Surface morphology images of HE-LKTO-3 coating after 300 s thermal shock by 1200 °C plasma jet: macroscopic morphology image (a); microscopic image of the central ablation zone (b); microscopic image of the transition ablation zone (c); microscopic image of the peripheral ablation zone (d); low magnification image of the transition ablation zone (e) and EDS mapping (f) of the rectangular boxed area.

at the edges drops off sharply, resulting in inadequate ablation. EDS mapping was conducted in the transition zone between central ablation and peripheral regions to analyze elemental redistribution across the thermal gradient. As shown in Fig. 8(f), the HE-LKTO-3 coating maintained uniform distribution of its five A-site metal elements after exposure to a plasma jet at 1400 °C, and there was no separation phenomenon, highlighting its extremely high thermal stability.

Fig. 9 reveals the ablation failure characteristics of the HE-LKTO-3 coating after extreme thermal shock under a 1600 °C plasma jet for 300 s. The macroscopic morphology (Fig. 9(a)) indicates severe overheating in the central ablated area, exhibiting localized coating spallation. As depicted in Fig. 9(b), the central ablation zone exhibits a prominent network of wide cracks, which primarily originated from the thermal stress generated during the shock process [46]. A higher-magnification view of the central region (Fig. 9(c)) reveals that, compared to the effects observed at 1400 °C, the 1600 °C thermal load triggered a more intense remelting-solidification cycle. The subsequently rapidly solidified melt developed a new, tightly interlocked and rugged microstructure.

3.3. Thermal protection performance and failure mechanism of the HE-LKTO-3 coating

Thermal insulation performance is the most critical service indicator for TPCs [9]. Therefore, evaluating the thermal insulation performance

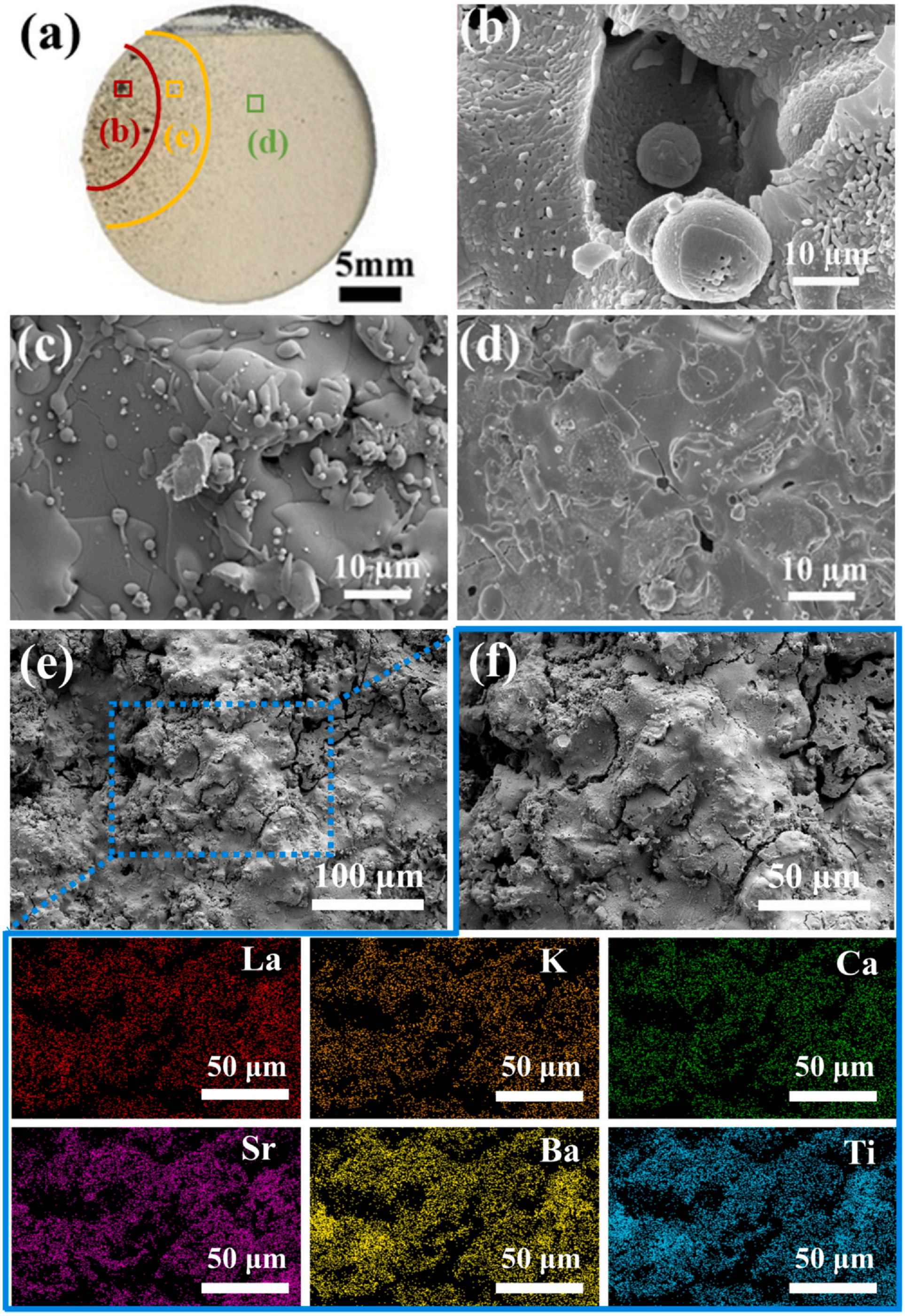

Fig. 8. Surface morphology images of HE-LKTO-3 coating after 300 s thermal shock by 1400 °C plasma jet: macroscopic morphology image (a); microscopic image of the central ablation zone (b); microscopic image of the transition ablation zone (c); microscopic image of the peripheral ablation zone (d); low magnification image of the transition ablation zone (e) and EDS mapping (f) of the rectangular boxed area.

of the HE-LKTO-3 coating under the four high-temperature thermal shock test conditions is crucial. During the thermal shock tests conducted using a high-temperature plasma jet, the surface and backside temperatures of the HE-LKTO-3 coating were monitored in real-time by an infrared thermography and thermocouples, respectively. The corresponding temperature curves are presented in Fig. 10. When the temperature difference between the front and back sides stabilized, a front surface temperature of 1000 °C resulted in a backside temperature of 540 °C. Subsequently, the backside temperature reached to 780 °C, 1050 °C, and 1380 °C as the front surface temperature increased to 1200 °C, 1400 °C, and 1600 °C, respectively. In other words, when the response temperature of the coating surface is 1000 °C, 1200 °C, 1400 °C, and 1600 °C, the corresponding insulation temperatures are 460 °C, 420 °C, 350 °C, and 220 °C, respectively. This data reveals a clear trend: as the temperature of the plasma flame impinging on the coating surface rises, the temperature differential across the HE-LKTO-3 sample progressively narrows. This change occurs because the intense and prolonged thermal and erosive forces induce surface melting and spallation of the coating. Such damage compromises the structural integrity of the coating and consequently degrades its thermal insulation performance. Liu et al. [47] prepared YSZ coating using APS technology, and found that the insulation temperature of the coating at 1200 °C was only 84 °C, much

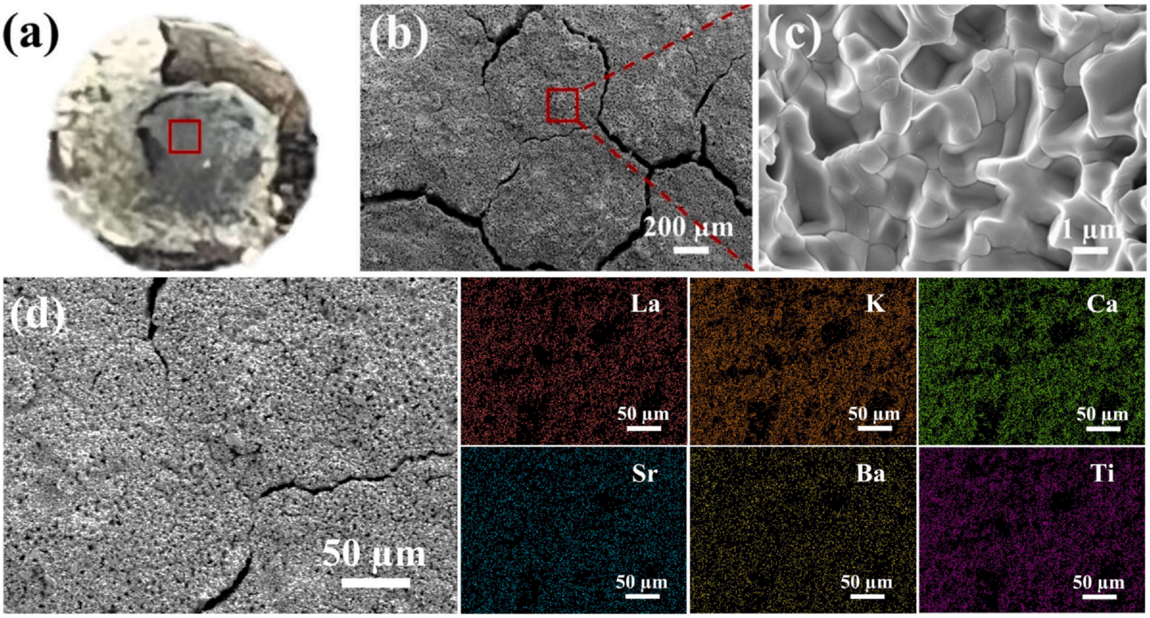

Fig. 9. Surface morphology images of HE-LKTO-3 coating after 300 s thermal shock by 1600 °C plasma jet: macroscopic morphology image (a); microscopic image of the central ablation zone (b); enlarged image of the central ablation zone (c) and surface elemental distribution map (d) of the coating.

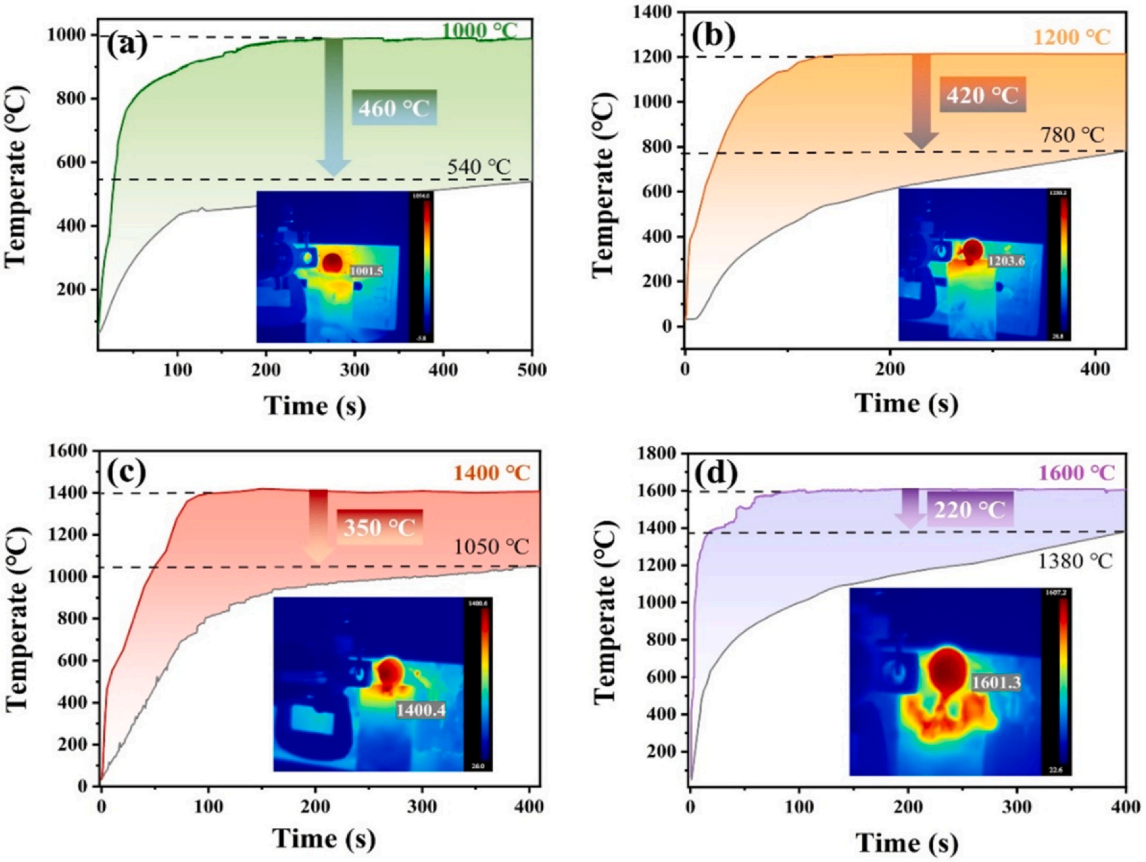

Fig. 10. Thermal insulation capability curve of the HE-LKTO-3 coating after 300 s of plasma flame thermal shock testing at 1000 °C (a), 1200 °C (b), 1400 °C (c) and 1600 °C (d).

lower than the insulation temperature of HE-LKTO-3 coating at the same temperature (420 °C). Chen et al. [48] used APS technology to prepare two types of YSZ coatings (submicron structure and nanostructure), both of which have thermal insulation performance lower than 100 °C at an ambient temperature of 1200 °C. Furthermore, YSZ coatings undergo a phase transformation at around 1200 °C, which is accompanied by a volume expansion of 3 – 5 % [49]. In other words, the failure temperature of YSZ coatings is essentially 1200 °C, whereas the failure temperature of the HE-LKTO-3 coating studied here reaches as high as 1600 °C.

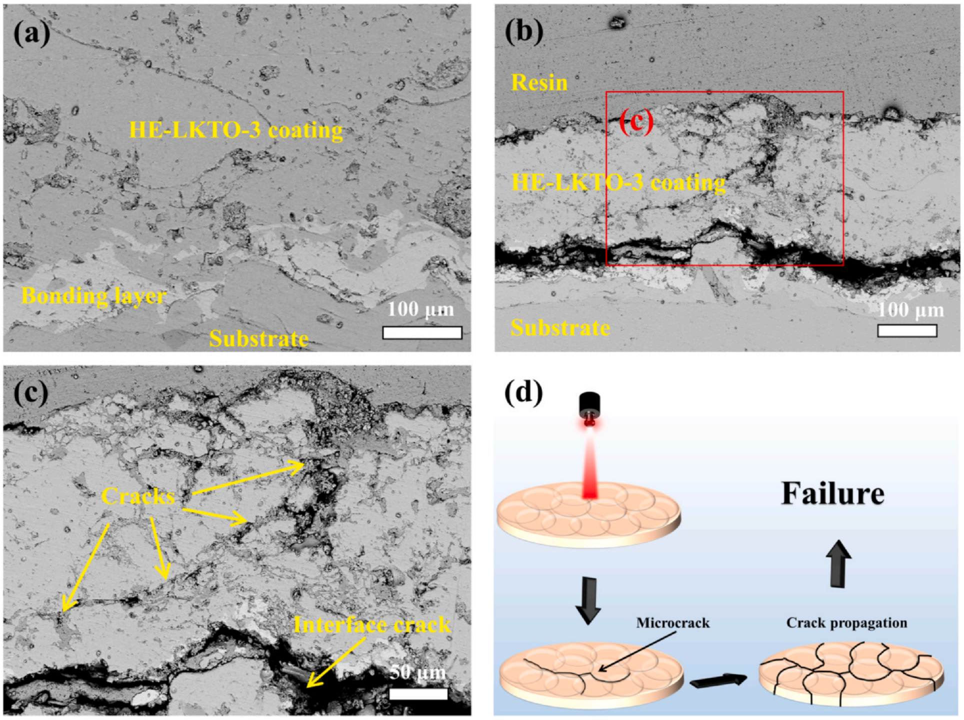

Fig. 11. Cross-section microstructures of HE-LKTO-3 coating under thermal shock test at 1400 ℃ (a) and 1600 ℃ (b)-(c). As well as the schematic diagram of the microstructure evolution process of the coating (d).

Fig. 11 displays SEM images of the cross-section of the HE-LKTO-3 coating after thermal shock testing. As shown in Fig. 11(a), after testing at 1400 ℃, the interfaces between the top coating, the bonding layer, and the substrate remain clear and well-bonded, with no obvious delamination observed. This result is consistent with the experimental finding that the coating maintains a high thermal insulation performance (with an insulation temperature drop of 350 ℃) at 1400 ℃, further confirming the significant potential of HE-LKTO as a novel high-entropy titanate TPC for high-temperature applications. This performance can be attributed primarily to the sluggish diffusion effects characteristic of high-entropy coatings, which impart properties such as sintering resistance [50] and low volumetric shrinkage [43]. These features help to release stress and allow pores to absorb crack-tip energy under thermal loading, thereby enhancing the coating's actual service life [6]. Additionally, the bonding layer, with its moderate thermal expansion coefficient (approximately $15 \times 10^{-6}\ \mathrm{K}^{-1}$) [51] and excellent ductility, acts as a “stress buffer”, effectively dissipating localized stress concentrations at the interface between the top coating and the substrate, thereby delaying interfacial cracking. In contrast, when the test temperature was increased to 1600 ℃ (as shown in Fig. 11(b), (c)), distinct interfacial separation between the top coating and the bonding layer occurred, accompanied by crack propagation along the interface. This is due to the aggravated mismatch in the thermal expansion coefficients between the top coating and the substrate under extreme temperatures, leading to significant thermal stress at the interface. As reported by Zhang et al. [41], such a thermal expansion coefficient gradient across the coating system induces radial and axial thermal stresses during plasma flame thermal shock, with tensile stress at high temperatures (1200 – 1600 ℃) and compressive stress during cooling. With continued thermal shock, these stresses accumulate at the interface, initiating and propagating microcracks. Under prolonged thermal shock, the bonding layer further accelerates coating failure through the accumulation of interfacial stresses. Furthermore, the cross-sectional images (Fig. 11(c)) reveal cracks penetrating through the coating thickness, resulting from stress concentration induced by rapid heating and cooling during thermal shock. The lamellar structure (formed by the APS process) of the coating weakens at high temperatures due to grain growth and sintering effects, reducing interlayer bonding strength and further promoting crack propagation along the interlamellar boundaries, ultimately leading to coating spallation.

Based on the above observations, the microstructural evolution of the HE-LKTO-3 coating during thermal shock testing can be divided into three stages (Fig. 11(d)): (i) Initiation of microcracks at the interface between the top coating and bonding layer driven by thermal mismatch stress; (ii) Propagation of cracks along the top coating/bonding layer interface as thermal shock continues. To effectively relieve interfacial stress and reduce the energy release rate at the crack tip, cracks penetrating the coating and secondary cracks are induced [52], leading to gradual weakening of the lamellar structure; (iii) Further extension and interconnection of cracks, eventually causing separation between the top coating and the bonding layer and resulting in failure of the coating.

4. Conclusion

In this study, HE-LKTO coatings were prepared using APS technology by varying the spraying power. Systematic investigations were conducted to elucidate the relationship between the coating’s microstructure, thermal protection performance, and failure mechanisms under plasma flame thermal shock. The results demonstrate that the as-sprayed coatings retain a single-phase solid solution structure with a dense, layered morphology. At a spraying power of 36 kW, the HE-LKTO-3 coating achieved the most favorable microstructural characteristics (such as minimum porosity). The exceptional thermal protection performance of the HE-LKTO-3 coating is attributed to its high-entropy nature. During thermal shock testing, the coating maintained integrity and effective thermal insulation up to 1400 ℃, with only localized ablation features observed. However, at an extreme temperature of 1600 ℃, the coating undergoes spallation failure due to accumulated thermal stress induced by the mismatched thermal expansion coefficients between the coating and substrate, as well as crack propagation along interlamellar boundaries and interface separation. This study offers valuable insights for the development of high-entropy titanate ceramic coatings and demonstrates their promising application in extreme thermal environments.

CRediT authorship contribution statement

Xiaofei Ma: Writing – original draft, Validation, Investigation. **Jinpeng Zhu:** Writing – review & editing, Validation, Investigation. **Chang Gao:** Methodology, Investigation. **Mingliang Li:** Investigation. **Hailong Wang:** Supervision, Resources. **Jilin He:** Supervision, Resources.

Declaration of Competing Interest

The authors declare that they have no known competing financial interests or personal relationships that could have appeared to influence the work reported in this paper.

Acknowledgements

The support from the National Natural Science Foundation of China (No. 52471099), the Project of Zhongyuan Critical Metals Laboratory (No. GJJSGFYQ202317), the Henan Province High-Level Young Talent Project (2022), and Henan Province University Science and Technology Innovation Talent Support Program (25HASTIT011).

References

[1] N.P. Padture, M. Gell, E.H. Jordan, Thermal Barrier Coatings for Gas-Turbine Engine Applications, Science 296 (2002) 280–284.
[2] Y. Liu, H. Wang, J. Hao, Y. Cheng, S. Dong, P. Hu, W. Han, X. Zhang, Key materials for extreme high-temperature environments: Ultra-high-temperature ceramics and their composites, Extrem. Mater. 1 (2025) 38–66.
[3] Q. Zhang, H. Zhang, M. Jiang, Q. Feng, C. Hu, Cyclic ablation mechanisms of Cr_2AlC ceramics in nitrogZhang Q.Zhang H.Jiang M.Feng Q.Hu C. Cyclic ablation mechanisms of Cr_2AlC ceramics in nitrogen plasma flame at 1600 °CExtrem. Mater.1202518en plasma flame at 1600 °C, Extrem. Mater. 3 (2025) 1–8.
[4] D. Zhou, D.E. Mack, E. Bakan, G. Mauer, D. Sebold, O. Guillon, R. Vaßen, Thermal cycling performances of multilayered yttria-stabilized zirconia/gadolinium zirconate thermal barrier coatings, J. Am. Ceram. Soc. 103 (2020) 2048–2061.
[5] D.R. Clarke, M. Oechsner, N.P. Padture, Thermal-barrier coatings for more efficient gas-turbine engines, MRS Bull. 37 (2012) 891–898.
[6] K. Wang, J. Zhu, H. Wang, K. Yang, Y. Zhu, Y. Qing, Z. Ma, L. Gao, Y. Liu, S. Wei, Y. Shu, Y. Zhou, J. He, Air plasma-sprayed high-entropy $(Y_{0.2}Yb_{0.2}Lu_{0.2}Eu_{0.2}Er_{0.2})_3Al_5O_{12}$ coating with high thermal protection performance, J. Adv. Ceram. 11 (2022) 1571–1582.
[7] C. Wu, S. Yi, L. Xu, J. Jing, Y. Ling, W. Lu, High-temperature oxidation behavior of (TiZrNbMoTa)N high entropy ceramic coating for dry cutting tools, Vacuum 233 (2025) 113897.
[8] H. Li, X. Luo, S. Huang, K. Li, S. Zhang, H. Jin, Potential thermal barrier coating material: High entropy ceramic $(Ca_{0.5}Sr_{0.5})(5RE)_2O_4$ with enhanced thermophysical properties, Ceram. Int. 49 (2023) 39627–39631.
[9] J. Tian, J. Zhu, J. Zheng, Y. Li, K. Yang, M. Li, H. Wang, J. He, Thermal protection mechanism of novel high-entropy rare-earth niobate coating deposited by atmospheric plasma spraying, Appl. Surf. Sci. 688 (2025) 162315.
[10] Y. Li, D. Pan, J. Cao, W. Fang, Y. Bao, B. Liu, Recent advances in high-entropy ceramics: Design principles, structural characteristics, and emerging properties, Extrem. Mater. 1 (2025) 42–72.
[11] C.M. Rost, E. Sachet, T. Borman, A. Moballegh, E.C. Dickey, D. Hou, J.L. Jones, S. Curtarolo, J.-P. Maria, Entropy-stabilized oxides, Nat. Commun. 6 (2015) 8485.
[12] Y. Wang, B. Mi, J. Wang, P. Liu, X. Ma, T. Chen, W. Li, Research progress on microstructure and properties of high entropy ceramic films and coatings, J. Mater. Res. Technol. 39 (2025) 1691–1719.
[13] J.W. Yeh, Alloy Design Strategies and Future Trends in High-Entropy Alloys, J. Miner. Met. Mater. Soc. 65 (2013) 1759–1771.
[14] K.Y. Tsai, M.H. Tsai, J.W. Yeh, Sluggish diffusion in Co–Cr–Fe–Mn–Ni high-entropy alloys, Acta Mater. 61 (2013) 4887–4897.
[15] J.W. Yeh, S.Y. Chang, Y.D. Hong, S.K. Chen, S.J. Lin, Anomalous decrease in X-ray diffraction intensities of Cu–Ni–Al–Co–Cr–Fe–Si alloy systems with multi-principal elements, Mater. Chem. Phys. 103 (2007) 41–46.
[16] S.T. Chen, W.Y. Tang, Y.F. Kuo, S.Y. Chen, C.H. Tsau, T.T. Shun, J.W. Yeh, Microstructure and properties of age-hardenable $Al_xCrFe_{1.5}MnNi_{0.5}$ alloys, Materials Science Engineering A 527 (2010) 5818–5825.
[17] J. Wu, X. Ma, X. Hu, L. Yan, F. Hou, J. Liu, A. Guo, New class of high-entropy pseudobrookite titanate with excellent thermal stability, low thermal expansion coefficient, and low thermal conductivity, J. Adv. Ceram. 11 (2022) 1654–1670.
[18] S. Zhu, J. Zhu, S. Ye, Y. Zhang, S. Zhang, K. Yang, M. Li, H. Zou, H. Wang, J. He, Ablation behavior and mechanisms of high-entropy rare earth titanates $(Y_{0.2}Gd_{0.2}Ho_{0.2}Er_{0.2}Yb_{0.2})_2Ti_2O_7$ coating deposited by plasma spraying technology, Surf. Coat. Technol. 478 (2024) 130414.
[19] A.A. Yaremchenko, S. Populoh, S.G. Patrício, J. Macías, P. Thiel, D.P. Fagg, A. Weidenkaff, J.R. Frade, A.V. Kovalevsky, Boosting Thermoelectric Performance by Controlled Defect Chemistry Engineering in Ta-Substituted Strontium Titanate, Chem. Mater. 27 (2015) 4995–5006.
[20] Y. Ohya, S. Yamamoto, T. Ban, M. Tanaka, S. Kitaoka, Thermal expansion and mechanical properties of self-reinforced aluminum titanate ceramics with elongated grains, J. Eur. Ceram. Soc. 37 (2017) 1673–1680.
[21] D. Hanifi, N. Hakimi, R. Ali, T. Huang, T. Huma, D. Bakhshyar, N.R. Afzali, M. Shafi, H. Babeker, J. Lu, P. Song, The fracture toughness and tribological performance of $NiAl/Al_2O_3$-40 wt% TiO_2 coating generated by air plasma spraying, Ceram. Int. 50 (2024) 1533–1546.
[22] C. Gao, J. Zhu, S. Ye, M. Li, H. Wang, J. He, Novel high-entropy perovskite titanate: A potential thermal protective material with improved thermophysical properties, J. Eur. Ceram. Soc. 45 (2025) 116878.
[23] L. Łatka, L. Pawłowski, M. Winnicki, P. Sokołowski, A. Małachowska, S. Kozerski, Review of Functionally Graded Thermal Sprayed Coatings, Appl. Sci. 10 (2020) 5153.
[24] K. Khantisopon, S. Singh, J. Jitputti, C.C. Berndt, A.S.M. Ang, High Temperature Corrosion Resistant and Anti-slagging Coatings for Boilers: A Review, High. Temp. Corros. Mater. 101 (2024) 1–55.
[25] S.H. Mirhosseini, M. Mosallaee, M. Razavi, M. Fotouhi, Reaction behavior and wear properties of in-situ air plasma-sprayed Al_2O_3-TiB_2 composite coatings, J. Eur. Ceram. Soc. 43 (2023) 6482–6492.
[26] J. Deng, Y. Qin, J. He, H. Zhao, Plasma-sprayed Ti-Si-C coatings and their crystallization behaviors depending on Ti powder content, Surf. Coat. Technol. 456 (2023) 129289.
[27] J. Zhang, J. Zhu, J. Zheng, Y. Li, S. Zhang, K. Wang, K. Yang, M. Li, H. Wang, J. He, High temperature thermal shock resistance of plasma-sprayed high-entropy $(Y_{0.2}Yb_{0.2}Ho_{0.2}Er_{0.2}Tm_{0.2})_2Hf_2O_7$ coating, J. Am. Ceram. Soc. 108 (2025) e20664.
[28] C. Kinsler-Fedon, L. Nuckols, C.T. Nelson, Z. Qi, Q. Huang, D. Mandrus, Y. Zhang, W.J. Weber, V. Keppens, Effects of Au^{2+} irradiation induced damage in a high-entropy pyrochlore oxide single crystal, Scr. Mater. 220 (2022) 114916.
[29] K. Yang, K. Bryce, W. Zhu, D. Zhao, J. Lian, Multicomponent pyrochlore solid solutions with uranium incorporation – A new perspective of materials design for nuclear applications, J. Eur. Ceram. Soc. 41 (2021) 2870–2882.
[30] C. Kinsler-Fedon, Q. Zheng, Q. Huang, E.S. Choi, J. Yan, H. Zhou, D. Mandrus, V. Keppens, Synthesis, characterization, and single-crystal growth of a high-entropy rare-earth pyrochlore oxide, Phys. Rev. Mater. 4 (2020) 104411.
[31] L. Zhang, Y. Li, X. Li, H. Yang, X. Qiao, T. Zhou, Z. Wang, J. Zhang, D. Tang, Characterization of spray granulated Nd:YAG particles for transparent ceramics, J. Alloy. Compd. 639 (2015) 244–251.
[32] P.-Y. Gao, Y.-D. Ma, W.-W. Sun, Y. Yang, C. Zhang, Y.-H. Cui, Y.-W. Wang, Y.-C. Dong, Microstructure and properties of Al_2O_3–ZrO_2–TiO_2 composite coatings prepared by plasma spraying, Rare Met. 40 (2021) 1825–1834.
[33] T.-K. Lin, D.-S. Wuu, S.-Y. Huang, W.-K. Wang, Characteristics of yttrium fluoride and yttrium oxide coatings for plasma process equipment prepared by atmospheric plasma spraying, Jpn. J. Appl. Phys. 55 (2016) 126201.
[34] J. Hu, P. Liu, Q. Li, J. Xie, S. Jiang, X. Jiang, X. Wang, L. Zhang, L. Yin, H. Lu, L. Deng, Influence of high-enthalpy atmospheric plasma spraying power on oxidation resistance of ZrB_2-LaF_3 coatings, Surf. Coat. Technol. 410 (2021) 126975.
[35] J. Feng, J. Wang, K. Yang, J. Rong, Microstructure and performance of $YTaO_4$ coating deposited by atmospheric plasma spraying on TC4 titanium alloy surface, Surf. Coat. Technol. 431 (2022) 128004.
[36] S.-Y. Chen, H.-D. Wang, G.-Z. Ma, J.-J. Kang, B.-S. Xu, Fractal and statistical properties of the geometrical structure of natural pores within plasma sprayed coatings, Acta Phys. Sin. 64 (2015).
[37] L. Li, F. Xie, X. Wu, J. He, S. Li, Microstructure and phase formation of atmospheric plasma sprayed YAG coatings, Surf. Coat. Technol. 466 (2023) 129614.
[38] L. Huang, R. Dou, Z. Wen, N. Liu, M. Yu, X. Liu, Microcrack Morphology in the Thermal Insulation Performance of 8YSZ Thermal Barrier Coatings: A Mesoscale Numerical Study, J. Therm. Spray. Technol. 32 (2023) 1115–1126.
[39] C. Oses, C. Toher, S. Curtarolo, High-entropy ceramics, Nat. Rev. Mater. 5 (2020) 295–309.
[40] T.-K. Tsao, A.-C. Yeh, C.-M. Kuo, H. Murakami, On The Superior High Temperature Hardness of Precipitation Strengthened High Entropy Ni-Based Alloys, Adv. Eng. Mater. 19 (2017) 1600475.
[41] Y. Zhang, J. Zhu, J. Zheng, K. Wang, Y. Li, K. Yang, M. Li, H. Wang, J. He, High-Temperature Thermal Protective Performance of High-Entropy Rare-Earth Tantalate $(Nd_{0.2}Dy_{0.2}Ho_{0.2}Y_{0.2}Er_{0.2})TaO_4$ Coating Deposited By Atmospheric Plasma Spraying, J. Therm. Spray. Technol. 34 (2025) 2483–2499.
[42] X. Gu, X.-B. Guo, W.-H. Li, Y.-P. Jiang, Q.-X. Liu, X.-G. Tang, High-Entropy Materials for Application: Electricity, Magnetism, and Optics, ACS Appl. Mater. Interfaces 16 (2024) 53372–53392.
[43] L. Zhou, F. Li, J.-X. Liu, Q. Hu, W. Bao, Y. Wu, X. Cao, F. Xu, G.-J. Zhang, High-entropy thermal barrier coating of rare-earth zirconate: A case study on $(La_{0.2}Nd_{0.2}Sm_{0.2}Eu_{0.2}Gd_{0.2})_2Zr_2O_7$ prepared by atmospheric plasma spraying, J. Eur. Ceram. Soc. 40 (2020) 5731–5739.
[44] J. Zhou, Z. He, Y. Ma, S. Dong, Study of light-absorbing crystal birefringence and electrical modulation mechanisms for coupled thermal-optical effects, Appl. Opt. 53 (2014) 6243–6255.

[45] Y.-J. Hsu, H.-Y. Wu, W.-C. Chang, Y.-T. Nien, Machining fused silica surface by continuous-wave CO_2 laser beams and their nanostructure characterizations, Mater. Lett. 306 (2022) 130960.

[46] X. Li, K. Yang, D. Wang, C. Deng, Y. Zhou, Property of TiO_2-15$MgAl_2O_4$ Electrical-Heating Coating Prepared by Atmospheric Plasma Spraying and Hydrogen Heat Treatment, Coatings 10 (2020) 177.

[47] Q. Liu, X.P. Hu, W. Zhu, G.L. Liu, J.W. Guo, J. Bin, Thermal shock performance and failure behavior of $Zr_6Ta_2O_{17}$-8YSZ double-ceramic-layer thermal barrier coatings prepared by atmospheric plasma spraying, Ceram. Int. 48 (2022) 24402–24410.

[48] D. Chen, F. Luo, X. Lou, Y. Qing, W. Zhou, D. Zhu, Comparison of thermal insulation capability between conventional and nanostructured plasma sprayed YSZ coating on Ni_3Al substrates, Ceram. Int. 43 (2017) 4324–4329.

[49] K. Leng, A.Rincon Romero, T. Hussain, Multilayer GZ/YSZ thermal barrier coating from suspension and solution precursor thermal spray, J. Eur. Ceram. Soc. 43 (2023) 4991–5003.

[50] Z. Zhao, H. Xiang, F.-Z. Dai, Z. Peng, Y. Zhou, $(La_{0.2}Ce_{0.2}Nd_{0.2}Sm_{0.2}Eu_{0.2})_2Zr_2O_7$: A novel high-entropy ceramic with low thermal conductivity and sluggish grain growth rate, J. Mater. Sci. Technol. 35 (2019) 2647–2651.

[51] Y. Wang, C. Wang, Y. You, W. Cheng, M. Dong, Z. Zhu, J. Liu, L. Wang, X. Zhang, Y. Wang, Analysis on thermal stress of optimized functionally graded coatings during thermal shock based on finite element simulation, Mater. Today Commun. 35 (2023) 105699.

[52] J. Zhu, Z. Ma, Y. Gao, L. Gao, V. Pervak, L. Wang, C. Wei, F. Wang, Ablation Behavior of Plasma-Sprayed $La_{1-x}Sr_xTiO_{3+\delta}$ Coating Irradiated by High-Intensity Continuous Laser, ACS Appl. Mater. Interfaces 9 (2017) 35444–35452.